AIAA JOURNAL
Vol. 38, No. 7, July 2000

Computational Fluid Dynamics Algorithms for Unsteady Shock-Induced Combustion, Part 1: Validation

Jeong-Yeol Choi*
Pusan National University, Pusan 609-735, Republic of Korea
and
In-Seuck Jeung† and Youngbin Yoon*
Seoul National University, Seoul 151-742, Republic of Korea

A computational study is carried out to develop a fully implicit and time-accurate computational fluid dynamics code for the analysis of reactive flow systems. Periodically oscillating shock-induced combustion around a blunt body in a stoichiometric hydrogen–air mixture is used as a validation problem of examining various numerical considerations. Euler equations and species conservation equations are used as the governing equations for the chemically reacting flow. Spatial discretization of the governing equation is based on Roe's approximate Riemann solver with a MUSCL-type total variation diminishing scheme for higher-order spatial resolution. The second-order-accurate time integration method is based on a lower–upper symmetric Gauss–Seidel scheme, using a Newton subiteration method and Steger–Warming flux Jacobian splitting. As a first step of the validation procedure, simulations of experimental results were carried out to confirm the reliability of the baseline method. In the next step, the general aspects of the baseline method were examined, including order of time integration, number of subiterations, and use of approximate flux Jacobian splitting. Appropriateness of the grid system is also examined by using a grid refinement study.

Introduction

SHOCK-INDUCED combustion is the self-ignited combustion phenomena of a premixed gas induced by the flight of a hypervelocity projectile in a combustible gas mixture. It has gained public interest as a promising combustion mechanism for hypersonic propulsion devices such as oblique detonation wave engine[1] and ram accelerators.[2] In addition to much experimental and theoretical research in the 1960s and 1970s, a computational fluid dynamics approach has been used as a major research tool of the phenomena in the 1980s and 1990s, with developments in numerical methods and computational power.

The shock-induced combustion flowfield is characterized by the hypersonic range flow velocity and the finite rate exothermic chemistry behind the bow shock. Thus, the coupling and the interaction between the bow shock and the reaction wave show the various and distinctive flow features according to the chemical and fluid dynamic conditions. Among the various features of shock-induced combustion, a periodically unstable regime would be the most interesting due to its naturally oscillating characteristics. Figure 1 is the shadowgraph of the unstable phenomena taken by Lehr[3] in the 1960s. After the experimental observations in 1960s and 1970s, many researchers showed their interest in the phenomena. The oscillating mechanism of shock-induced combustion was suggested by Toongs[4] in the 1970s and was proved numerically by Matsuo and Fujiwara[5] and Matsuo et al.[6] in 1990s as a wave interaction mechanism between the shock wave, combustion wave, compression and expansion waves, and projectile surface.

For the analysis of the unsteady combustion phenomena, a stable and time-accurate numerical approach is required to capture the strong bow shock and weak pressure waves without numerical instability or distortion because the phenomena is the result of wave interactions between the bow shock, combustion wave, and body surface. In addition, a detailed combustion mechanism that includes a sufficient number of chemical species and elementary reaction steps should be used to reproduce accurately the experimental results of shock standoff distance, induction distance, and oscillation frequency because these characteristics are determined by finite rate reaction mechanisms. The inclusion of more species results in the increase of the variables proportional to the number of species and the increase of the matrix inversion time proportional to the cubic number of equations. Moreover, a huge grid system is also needed to resolve the wave interactions between bow shock and body surface. Therefore, enormously large memory capacity and computing time seem to be inevitable for the analysis of the unsteady combustion phenomena. The reliable simulation results of the oscillating combustion phenomena began to appear in the 1990s with the help of developments in numerical methods and computational power.[5–7] At present, the development of computing power makes the simulation possible on a desktop computer, and the numerical approach is used in the analysis of the unknown shock-induced combustion phenomena for which the experimental or analytic methods do not apply adequately.[5,6]

During the past several years, many researchers performed simulations of experimentally known shock-induced combustion and reproduced the experimental result with sufficient accuracy.[5–9] However, there are some discrepancies between their simulations and experimental results because they used different numerical methods and computational conditions. They explained the discrepancies by the inaccuracies of the chemistry mechanisms, numerical methods, etc. However, the huge computational expense of the analysis prevented the needed validational or comparative studies before using the computational methods in the analysis of unknown physical problems.

In this study, a comparative study of numerical methods is made as a part of the process of developing an efficient computational fluid dynamics code capable of analyzing unsteady reacting flows. A time-accurate fully implicit algorithm and a third-order spatially accurate upwind scheme are presented as baseline methods. Validation of these baseline methods is made with the simulation of experimental results, and then the results from different numerical approaches are compared with those of the baseline method.

Presented as Paper 98-3217 at the AIAA/ASME/SAE/ASEE 34th Joint Propulsion Conference, Cleveland, OH, 13–15 July 1998; received 14 January 1999; revision received 13 December 1999; accepted for publication 29 December 1999.

*Assistant Professor, Department of Aerospace Engineering. Member AIAA.

†Professor, Department of Aerospace Engineering. Senior Member AIAA.

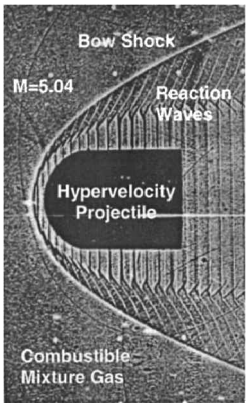

Fig. 1 Experimental shadowgraph of periodically oscillating shock-induced combustion.[3]

Governing Equation and Chemistry Mechanism

The oscillatory phenomena in shock-induced combustion are basically due to the interaction between the shock and the combustion wave. The effect of transport properties is known to be negligible.[4] Therefore, species conservation equations and inviscid Euler equations are used as governing equations of the reacting flow around an axisymmetric blunt body. The conservation form of these governing equations set involving N number of species is written in curvilinear coordinate form as follows:

$$\frac{\partial \boldsymbol{Q}}{\partial t} + \frac{\partial \boldsymbol{F}}{\partial \xi} + \frac{\partial \boldsymbol{G}}{\partial \eta} + \boldsymbol{H} = \boldsymbol{W} \tag{1}$$

where

$$\boldsymbol{Q} = \frac{1}{J}\begin{bmatrix} \rho_1 \\ \vdots \\ \rho_N \\ \rho u \\ \rho v \\ e \end{bmatrix}, \qquad \boldsymbol{F} = \frac{1}{J}\begin{bmatrix} \rho_1 U \\ \vdots \\ \rho_N U \\ \rho u U + \xi_x p \\ \rho v U + \xi_y p \\ (e+p)U \end{bmatrix}$$

$$\boldsymbol{G} = \frac{1}{J}\begin{bmatrix} \rho_1 V \\ \vdots \\ \rho_N V \\ \rho u V + \eta_x p \\ \rho v V + \eta_y p \\ (e+p)V \end{bmatrix}, \qquad \boldsymbol{H} = \frac{1}{yJ}\begin{bmatrix} \rho_1 v \\ \vdots \\ \rho_N v \\ \rho u v \\ \rho v^2 \\ (e+p)v \end{bmatrix}$$

$$\boldsymbol{W} = \frac{1}{J}\begin{bmatrix} w_1 \\ \vdots \\ w_N \\ 0 \\ 0 \\ 0 \end{bmatrix} \tag{2}$$

Here, u and v are the velocity components in Cartesian coordinates x and y, and U and V are the contravariant velocity components in the generalized coordinates:

$$U = \xi_x u + \xi_y v, \qquad V = \eta_x u + \eta_y v \tag{3}$$

Coordinate transformation metrics ξ_x, ξ_y, η_x, and η_y and metric Jacobian J are obtained from coordinate transform relation as follows:

$$J = 1/(x_\xi y_\eta - x_\eta y_\xi) \tag{4}$$

$$\xi_x = J y_\eta, \qquad \xi_y = -J x_\eta, \qquad \eta_x = -J y_\xi, \qquad \eta_y = J x_\xi \tag{5}$$

Total density ρ is expressed as a sum of the partial density ρ_k of each species:

$$\rho = \sum_{k=1}^{N} \rho_k \tag{6}$$

Pressure p is evaluated from the ideal gas law for a mixture of thermally perfect gases, and total energy per unit volume e is defined as a sum of kinetic energy and internal energy. The definition of total energy is used for the implicit evaluation of temperature T by the Newton–Raphson iteration method:

$$p = \sum_{k=1}^{N} \frac{\rho_k}{M_k} RT \tag{7}$$

$$e = \frac{\rho}{2}(u^2 + v^2) + \sum_{k=1}^{N} \rho_k \left(\int^T \frac{C_{pk} - R}{M_k}\,\mathrm{d}T + h_k^0 \right) \tag{8}$$

Here, M_k is the molecular weight for kth species and R is the universal gas constant. The specific heats of each species are obtained as functions of temperature from NASA thermochemical polynomial data that are valid up to 6000 K (Ref. 10):

$$C_{pk}/R = a_{1k} + a_{2k}T + a_{3k}T^2 + a_{4k}T^3 + a_{5k}T^4 \tag{9}$$

For the elementary reaction steps generally expressed as

$$\sum_{k=1}^{N} \nu'_{k,r} X_k \leftrightarrow \sum_{k=1}^{N} \nu''_{k,r} X_k \tag{10}$$

the mass production rate of each species in Eq. (2) is written as

$$w_k = M_k \sum_{r=1}^{Nr} (\nu''_{k,r} - \nu'_{k,r}) \left[k_{\mathrm{fr}} \prod_{k=1}^{N} \left(\frac{\rho_k}{M_k} \right)^{\nu'_{k,r}} - k_{\mathrm{br}} \prod_{k=1}^{N} \left(\frac{\rho_k}{M_k} \right)^{\nu''_{k,r}} \right] \tag{11}$$

where forward reaction rate constant k_{fr} for the rth reaction step is expressed in Arrhenius form:

$$k_{\mathrm{fr}} = A_r T^{B_r} \exp\left(-E_r^* / RT\right) \tag{12}$$

The reaction coefficients A_r, B_r, and activation energy E_r^* in Eq. (12) are taken from Jachimowski's detailed chemistry mechanisms for hydrogen–air combustion[11] (see Table 1). The original mechanism includes the oxidation process of nitrogen, but the reaction steps are

Table 1 Jachimowski's mechanisms for hydrogen–air combustion without nitrogen oxidation process[a]

Reaction	A_r	B_r	E_r^*
Forward reaction rate coefficients			
$H_2 + O_2 \leftrightarrow HO_2 + H$	1.00×10^{14}	0.00	56,000
$H + O_2 \leftrightarrow OH + O$	2.60×10^{14}	0.00	16,800
$O + H_2 \leftrightarrow OH + H$	1.80×10^{10}	1.00	8,900
$OH + H_2 \leftrightarrow H_2O + H$	2.20×10^{13}	0.00	5,150
$OH + OH \leftrightarrow H_2O + O$	6.30×10^{12}	0.00	1,090
$H + OH + X \leftrightarrow H_2O + X$	2.20×10^{22}	−2.00	0
$H + H + X \leftrightarrow H_2 + X$	6.40×10^{17}	−1.00	0
$H + O + X \leftrightarrow OH + X$	6.00×10^{16}	−0.60	0
$H + O_2 + X \leftrightarrow HO_2 + X$	2.10×10^{15}	0.00	−1,000
$HO_2 + H \leftrightarrow OH + OH$	1.40×10^{14}	0.00	1,080
$HO_2 + H \leftrightarrow H_2O + O$	1.00×10^{13}	0.00	1,080
$HO_2 + O \leftrightarrow O_2 + OH$	1.50×10^{13}	0.00	950
$HO_2 + OH \leftrightarrow H_2O + O_2$	8.00×10^{12}	0.00	0
$HO_2 \leftrightarrow H_2O_2 + O_2$	2.00×10^{12}	0.00	0
$H + H_2O_2 \leftrightarrow H_2 + HO_2$	1.40×10^{12}	0.00	3,600
$O + H_2O_2 \leftrightarrow OH + HO_2$	1.40×10^{13}	0.00	6,400
$OH + H_2O_2 \leftrightarrow H_2O + HO_2$	6.10×10^{12}	0.00	1,430
$H_2O_2 + X \leftrightarrow OH + OH + X$	1.20×10^{17}	0.00	45,500
$O + O + X \leftrightarrow O_2 + X$	6.00×10^{13}	0.00	−1,800
Third-body efficiencies relative to N_2			
$H + OH + X \leftrightarrow H_2O + X$	$H_2O = 6.0$		
$H + H + X \leftrightarrow H_2 + X$	$H_2O = 6.0$, $H_2 = 2.0$		
$H + O + X \leftrightarrow OH + X$	$H_2O = 6.0$		
$H + O_2 + X \leftrightarrow HO_2 + X$	$H_2O = 6.0$, $H_2 = 2.0$		
$H_2O_2 + X \leftrightarrow H + OH + X$	$H_2O = 15.0$		

[a]Units of reaction constants are seconds, moles, cubic centimeters, calories, and Kelvin.

neglected and nitrogen is assumed to be an inert species because the oxidation process does not have a significant effect on the fluid dynamics of shock-induced combustion. This combustion model has been successfully used and validated in a number of supersonic reacting flow studies.[5,7,8,11]

Backward reaction rate constant k_{br} in Eq. (11) is evaluated from the forward reaction rate constant and equilibrium constant:

$$K_{eq}^{r} = k_{fr}/k_{br} \tag{13}$$

The equilibrium constant is calculated from the Gibbs free-energy minimum condition as follows:

$$K_{eq}^{r} = \left(\frac{1\text{ atm}}{RT}\right)^{\sum_{k=1}^{N}(\nu''_{k,r}-\nu'_{k,r})} \exp\left[\sum_{k=1}^{N}(\nu''_{k,r}-\nu'_{k,r})\left(\frac{S_k^0}{R}-\frac{H_k}{RT}\right)\right] \tag{14}$$

Here, entropy S_k^0 and enthalpy H_k are obtained as functions of temperature from the specific heat data at standard state:

$$\frac{H_k}{RT} = \frac{1}{RT}\left\{\int^{T} C_{pk}\,\mathrm{d}T + H_{fk}^0\right\} \tag{15}$$

$$\frac{S_k^0}{R} = \int^{T}\frac{\mathrm{d}H_k}{RT} = \int^{T}\frac{C_{pk}\,\mathrm{d}T}{RT} \tag{16}$$

Baseline Numerical Method

Time-Accurate Implicit Integration with Newton Subiteration

A fully implicit second-order-accurate time-integration method is used for the analysis of an unsteady supersonic reacting flow. A Newton subiteration method is used to reduce the error of temporal discretization and to ensure the second-order time accuracy and stability in the case of a large time step equivalent to Courant–Friedrichs–Lewy (CFL) number greater than one. By the taking of the second-order approximation of time derivative and applying Newton's method to evaluate conservative variables at the next time step, the governing equation (1) could be written in discretized form as follows:

$$\left(c_0\boldsymbol{I} - \left(\frac{\partial \boldsymbol{R}}{\partial \boldsymbol{Q}}\right)\right)_{i,j}^{n+1,m} \Delta\boldsymbol{Q}_{i,j}^{n+1,m} = \boldsymbol{RHS}_{i,j}^{n+1,m}$$

$$\boldsymbol{RHS}_{i,j}^{n+1,m} = -c_0\boldsymbol{Q}_{i,j}^{n+1,m} - c_1\boldsymbol{Q}_{i,j}^{n} - c_2\boldsymbol{Q}_{i,j}^{n-1} + \boldsymbol{R}\left(\boldsymbol{Q}_{i,j}^{n+1,m}\right) \tag{17}$$

where the residual vector based on finite volume discretization is

$$\boldsymbol{R}_{i,j} = \boldsymbol{W}_{i,j} - \boldsymbol{H}_{i,j} - \tilde{\boldsymbol{F}}_{i+\frac{1}{2},j} + \tilde{\boldsymbol{F}}_{i-\frac{1}{2},j} - \tilde{\boldsymbol{G}}_{i,j+\frac{1}{2}} + \tilde{\boldsymbol{G}}_{i,j-\frac{1}{2}} \tag{18}$$

Conservative variables are updated from the evaluated increment at every time-integration level and subiteration step:

$$\boldsymbol{Q}_{i,j}^{n+1,m+1} = \boldsymbol{Q}_{i,j}^{n+1,m} + \Delta\boldsymbol{Q}_{i,j}^{n+1,m} \tag{19}$$

In this time-integration scheme, n is the designation of time-integration level and m is that of the sub-iteration step. Time marching is performed by assuming that the initial guess of the conservative variable at $n+1$ time level $\boldsymbol{Q}^{n+1,0}$ is $\boldsymbol{Q}^{n}$. In Eq. (17) c_0, c_1, and c_2 are the functions of time step size Δt^n, which is defined as

$$\Delta t^n = t^{n+1} - t^n \tag{20}$$

This time-integration scheme is second-order-accurate for arbitrary time step size by selecting c_0, c_1, and c_2 as

$$c_0 = \frac{1-\sigma}{(1-\sigma)\Delta t^n + \Delta t^{n-1}}, \qquad c_1 = \frac{\sigma}{(1-\sigma)\Delta t^n + \Delta t^{n-1}}$$

$$c_2 = \frac{-1}{(1-\sigma)\Delta t^n + \Delta t^{n-1}}, \qquad \sigma = \left(1 + \frac{\Delta t^{n-1}}{\Delta t^n}\right)^2 \tag{21}$$

Equation (21) can be first-order accurate by choosing

$$c_0 = 1/\Delta t^n, \qquad c_1 = -c_0, \qquad c_2 = 0 \tag{22}$$

The implicit part of Eq. (17) constitutes a block pentadiagonal system of equations. Alternating direction implicit schemes based on approximate factorization are often used for solving these kinds of pentadiagonal systems, but their efficiency degrades severely when the number of equations is very large. Thus, a lower–upper (LU) relaxation scheme[12] is used in this study that involves only pointwise matrix inversion. By applying the upwind discretization of flux Jacobian matrices, Eq. (17) can be rewritten in the following factorized form:

$$\boldsymbol{D} = c_0\boldsymbol{I} + (\boldsymbol{A}^{+} - \boldsymbol{A}^{-} + \boldsymbol{B}^{+} - \boldsymbol{B}^{-} - \boldsymbol{Z})_{i,j}$$

$$\boldsymbol{L} = \boldsymbol{D} - \boldsymbol{A}_{i-1,j}^{+} - \boldsymbol{B}_{i,j-1}^{+}, \qquad \boldsymbol{U} = \boldsymbol{D} + \boldsymbol{A}_{i+1,j}^{-} + \boldsymbol{B}_{i,j+1}^{-}$$

$$\boldsymbol{L}\boldsymbol{D}^{-1}\boldsymbol{U}\Delta\boldsymbol{Q}_{i,j} = \boldsymbol{RHS}_{i,j} \tag{23}$$

Here $\boldsymbol{A}^{\pm}$ and $\boldsymbol{B}^{\pm}$ are split Jacobian matrices of flux vectors $\boldsymbol{F}$ and $\boldsymbol{G}$, and $\boldsymbol{Z}$ is the Jacobian matrix of chemical source vector $\boldsymbol{W}$. The preceding LU-factored governing equation is actually inverted by the following two steps of the symmetric Gauss–Seidel method with a well-known LU-decomposition method for linear algebraic equations:

$$\boldsymbol{D}_{i,j}\Delta\boldsymbol{Q}_{i,j}^{*} = \boldsymbol{RHS}_{i,j} + \boldsymbol{A}_{i-1,j}^{+}\Delta\boldsymbol{Q}_{i-1,j}^{*} + \boldsymbol{B}_{i,j-1}^{+}\Delta\boldsymbol{Q}_{i,j-1}^{*}$$

$$\boldsymbol{D}_{i,j}\Delta\boldsymbol{Q}_{i,j}^{**} = -\boldsymbol{A}_{i+1,j}^{-}\Delta\boldsymbol{Q}_{i+1,j}^{n+1,m} - \boldsymbol{B}_{i,j-1}^{-}\Delta\boldsymbol{Q}_{i,j-1}^{n+1,m}$$

$$\Delta\boldsymbol{Q}_{i,j}^{n+1,m} = \Delta\boldsymbol{Q}_{i,j}^{*} + \Delta\boldsymbol{Q}_{i,j}^{**} \tag{24}$$

Among several choices available in evaluating a split flux Jacobian matrix, the Steger–Warming flux splitting method and an approximate splitting method are used in this study. Because these methods involve only a pointwise Jacobian matrix and do not involve neighboring points, evaluation of the left- and right-hand sides ($\boldsymbol{RHS}$) in Eq. (24) could be carried out in a much more simplified manner by the following manipulation of the flux Jacobian matrix.

In case of the Steger–Warming approach, the flux Jacobian matrix is split as

$$\boldsymbol{A}^{\pm} = \boldsymbol{R}\boldsymbol{\Lambda}^{\pm}\boldsymbol{R}^{-1}, \qquad \boldsymbol{\Lambda}^{\pm} = (\Lambda \pm |\boldsymbol{\Lambda}|)/2 \tag{25}$$

Here, $\boldsymbol{R}$ and $\boldsymbol{R}^{-1}$ are the left and right eigenvector matrix and $\boldsymbol{\Lambda}$ is the eigenvector having λ_1, λ_2, and λ_3 as different eigenvalues. The eigenvalues are defined as

$$\lambda_1 = U, \qquad \lambda_{2,3} = U \pm a\sqrt{\xi_x^2 + \xi_y^2} \tag{26}$$

The flux Jacobian matrix is reconstructed in the following form:

$$\boldsymbol{A} = \boldsymbol{R}\boldsymbol{\Lambda}\boldsymbol{R}^{-1} = \boldsymbol{A}' + \lambda_1\boldsymbol{I} \tag{27}$$

where

$$A' = \begin{bmatrix} p_{\rho_1}\frac{y_k}{a^2}\phi - \frac{y_k U}{a}\psi & -\frac{p_e u}{a^2}y_k\phi + \frac{\xi_x}{a}\psi & -\frac{p_e v}{a^2}y_k\phi + \frac{\xi_y}{a}\psi & \frac{p_e}{a^2}y_k\phi \\ \left(\frac{up_{\rho_1}}{a^2} - \xi_x U\right)\phi + \left(\frac{\xi_x p_{\rho_1} - uU}{a}\right)\psi & \left(\xi_x^2 - \frac{p_e u^2}{a^2}\right)\phi + (2-\bar{\gamma})\frac{u}{a}\xi_x\psi & \left(\xi_x\xi_y - \frac{p_e uv}{a^2}\right)\phi + \frac{(\xi_x v - \xi_y p_e u)}{a}\psi & \frac{p_e u}{a^2}\phi + \frac{p_e\xi_x}{a}\psi \\ \left(\frac{vp_{\rho_1}}{a^2} - \xi_y U\right)\phi + \frac{\left(\xi_y p_{\rho_1} - vU\right)}{a}\psi & \left(\xi_x\xi_y - \frac{p_e uv}{a^2}\right)\phi + \frac{(\xi_x v - \xi_y p_e u)}{a}\psi & \left(\xi_y^2 - \frac{p_e v^2}{a^2}\right)\phi + \frac{\xi_y v(2-\bar{\gamma})}{a}\psi & \frac{p_e v}{a^2}\phi + \frac{p_e\xi_y}{a}\psi \\ \left(\frac{Hp_{\rho_1}}{a^2} - U^2\right)\phi + \frac{U\left(p_{\rho_1} - H\right)}{a}\psi & \left(U\xi_x - \frac{up_e H}{a^2}\right)\phi + \frac{(\xi_x H - up_e U)}{a}\psi & \left(U\xi_y - \frac{vp_e H}{a^2}\right)\phi + \frac{(\xi_y H - vp_e U)}{a}\psi & \frac{p_e H}{a^2}\phi + \frac{p_e U}{a}\psi \end{bmatrix}$$

$$k = 1, \ldots, N \quad \text{and} \quad l = 1, \ldots, N \tag{28}$$

$$\phi = [(\lambda_2 + \lambda_3)/2] - \lambda_1, \qquad \psi = (\lambda_2 + \lambda_3)/2 \tag{29}$$

Here, p_e and p_{ρ_k} are the derivatives of pressure with respect to total energy and partial density. All of the metrics in Eq. (29) are used after normalization.

With this reconstructed form of the flux Jacobian matrix, the difference term of the Jacobian matrix in the diagonal matrix of Eq. (24) is simply evaluated by replacing the eigenvalues in Eqs. (27) and (29) by their absolute values:

$$\boldsymbol{A}^+ - \boldsymbol{A}^- = \boldsymbol{R}|\boldsymbol{\Lambda}|\boldsymbol{R}^{-1} = \boldsymbol{A}'(|\lambda_{1,2,3}|) + |\lambda_1|\boldsymbol{I} \tag{30}$$

More beneficially, the matrix and vector product terms in Eq. (24) can be evaluated by the following formulation in vector form:

$$\boldsymbol{A}^{\pm}\Delta\boldsymbol{Q} = \boldsymbol{A}(|\lambda_{1,2,3}|)\Delta\boldsymbol{Q} + |\lambda_1|\Delta\boldsymbol{Q}$$

$$= \begin{bmatrix} y_1 E + F + |\lambda_1| \\ \vdots \\ y_N E + F + |\lambda_1| \\ \left(\frac{u\phi}{a^2} + \frac{\xi_x\psi}{a}\right)A + \left(\phi\xi_x + \frac{u\psi}{a}\right)B + |\lambda_1| \\ \left(\frac{v\phi}{a^2} + \frac{\xi_y\psi}{a}\right)A + \left(\phi\xi_y + \frac{v\psi}{a}\right)B + |\lambda_1| \\ \left(\frac{H\phi}{a^2} + \frac{U\psi}{a}\right)A + \left(\phi U + \frac{H\psi}{a}\right)B + |\psi_1| \end{bmatrix}$$

$$A = \sum_{k=1}^{N} p_{\rho_k}\Delta q_k + p_e(-u\Delta q_{n1} - v\Delta q_{n2} + \Delta q_{n3})$$

$$D = U\sum_{k=1}^{N}\Delta q_k, \qquad C = \xi_x\Delta q_{n1} + \xi_y\Delta q_{n2}$$

$$B = \xi_x\Delta q_{n1} + \xi_y\Delta q_{n2} - U\sum_{k=1}^{N}\Delta q_k = C - D$$

$$E = \frac{\phi}{a^2}A - \frac{\psi}{a}D, \qquad F = \frac{\psi}{a}C \tag{31}$$

This matrix–vector product formulation is an exact one and saves a lot of computing time because this formulation is much more efficient than the matrix–vector product calculation.

MUSCL-Type Total Variation Diminishing Scheme Based on Roe's Flux Difference Splitting

The finite volume cell-vertex scheme is used for spatial discretization of governing equations. The convective terms in Eq. (18) are expressed as differences of numerical fluxes at cell interfaces. The numerical fluxes containing artificial dissipation are formulated using Roe's flux difference splitting (FDS) method[13]:

$$\tilde{\boldsymbol{F}}_{i+\frac{1}{2},j} = \tfrac{1}{2}[\boldsymbol{F}(\boldsymbol{Q}_R) + \boldsymbol{F}(\boldsymbol{Q}_L) - |\boldsymbol{A}(\boldsymbol{Q}_R, \boldsymbol{Q}_L)|(\boldsymbol{Q}_R - \boldsymbol{Q}_L)] \tag{32}$$

where subscript $\boldsymbol{L}$ and $\boldsymbol{R}$ imply the extrapolated values at the left and right grid points of cell interface. $\boldsymbol{A}(\boldsymbol{Q}_R, \boldsymbol{Q}_L)$ implies that the Jacobian matrix $\boldsymbol{A}$ is evaluated by the Roe's average of $\boldsymbol{Q}_R$ and $\boldsymbol{Q}_L$. Although there are various derivations of Roe's FDS method for multispecies chemically reacting flow such as Harten–Yee total variation diminishing (TVD) schemes,[14] and these methods also show good shock-capturing characteristics, the characteristic variable approach of Grossman and Cinnella[15] is used in this study and extended to two-dimensional curvilinear coordinates because only the characteristic variable approach satisfies the definition of the approximate Riemann solver and presents numerical flexibility of artificial damping control. By following the primitive variable approach used by Grossman and Cinnella[15] for the interface Jacobian matrix, the artificial dissipation term for chemically reacting flow can be written in two-dimensional curvilinear coordinate as follows:

$$|\boldsymbol{A}(\hat{\boldsymbol{Q}})|\delta\boldsymbol{Q} = \boldsymbol{R}|\Lambda|\boldsymbol{R}^{-1}\delta\boldsymbol{Q} = \sum_{l=1}^{4}|\delta\boldsymbol{F}|_l\,\delta w_l \tag{33}$$

where

$$|\delta\boldsymbol{F}|_1 = \begin{bmatrix} \hat{y}_1 \\ \vdots \\ \hat{y}_N \\ \hat{u} \\ \hat{v} \\ \hat{H} - \frac{\hat{a}^2}{\hat{p}_e} \end{bmatrix}$$

$$|\delta\boldsymbol{F}|_2 = \begin{bmatrix} \delta y_1 \\ \vdots \\ \delta y_N \\ \delta u - \xi_x\delta U \\ \delta v - \xi_y\delta V \\ (\xi_x\delta v - \xi_y\delta u)(\xi_x\hat{v} - \xi_y\hat{u}) - \frac{1}{\hat{p}_e}\sum_{k=1}^{N}\hat{p}_{\rho_k}\delta y_k \end{bmatrix}$$

$$|\delta\boldsymbol{F}|_{3,4} = \begin{bmatrix} \hat{y}_1 \\ \vdots \\ \hat{y}_N \\ \hat{u} \pm \xi_x\hat{a} \\ \hat{v} \pm \xi_y\hat{a} \\ \hat{H} \pm \hat{a}\hat{U} \end{bmatrix} \tag{34}$$

$$\delta w_1 = \psi(\lambda)\left(\delta\rho - \frac{\delta p}{\hat{a}^2}\right), \qquad \delta w_2 = \psi(\lambda_1)\hat{\rho}$$

$$\delta w_{3,4} = \psi(\lambda_{2,3})\left(\frac{\delta p \pm \hat{\rho}\hat{a}\,\delta U}{2\hat{a}^2}\right) \tag{35}$$

where $(\hat{})$ implies the Roe's averaged value at cell interface and $\delta(\,)$ means the difference of the extrapolated values at the left and right grid points. Grid metrics ξ_x and ξ_y are used after normalization.

Because Roe's FDS method does not satisfy the second law of thermodynamics, its solution sometimes shows unphysical solutions such as the carbuncle phenomena. As a remedy of such problems, the entropy fixing function by Montagne et al.[16] is used in the present study. In Eq. (35), $\psi(\lambda)$ is the corrected eigenvalue as follows:

$$\psi(\lambda) = \begin{cases} |\lambda|, & |\lambda| > \varepsilon \\ (\lambda^2 + \varepsilon^2)/2\varepsilon, & |\lambda| < \varepsilon \end{cases} \tag{36}$$

$$\varepsilon = \tilde{\varepsilon}[|\nabla\xi||U| + |\nabla\eta||V| + (a/2)(|\nabla\xi| + |\nabla\eta|)]_{i+\frac{1}{2},j} \tag{37}$$

Small number $\tilde{\varepsilon}$, which is typically used in the range of $0.01 \leq \tilde{\varepsilon} \leq 0.1$, is known to affect the artificial dissipation, the shock thickness, and the convergence rate,[16] but a large value $\tilde{\varepsilon} = 0.4$ was used as a reference value in the present study to ensure the solution stability.

As a higher-order extension of the upwind scheme, the MUSCL scheme is used for the extrapolation of primitive variables at the cell interface.[17] A limiter function is also used to overcome the severe dispersion error introduced by the higher-order extrapolation and to preserve the TVD property.[17] Using a minmod limiter, the extrapolated variables at the cell interfaces are expressed as

$$q_L = q_i + \tfrac{1}{4}\left[(1-\eta)\nabla_{i-\frac{1}{2}} + (1+\eta)\Delta_{i+\frac{1}{2}}\right]$$

$$q_R = q_{i+1} - \tfrac{1}{4}\left[(1+\eta)\nabla_{i+\frac{1}{2}} + (1-\eta)\Delta_{i+\frac{3}{2}}\right] \tag{38}$$

where

$$\Delta_{i+\frac{1}{2}} = \text{minmod}\left(\delta_{i+\frac{1}{2}}, \beta\delta_{i-\frac{1}{2}}\right)$$

$$\nabla_{i+\frac{1}{2}} = \text{minmod}\left(\delta_{i+\frac{1}{2}}, \beta\delta_{i+\frac{3}{2}}\right)$$

$$\delta_{i+\frac{1}{2}} = q_{i+1} - q_i \tag{39}$$

$$\text{minmod}(x, y) = \text{sign}(x) \cdot \max[0, \min\{|x|, y \cdot \text{sign}(x)\}] \tag{40}$$

where q_i is any primitive variable at grid point (i, j). The minmod function preserves the TVD property in the range of

$$1 \leq \beta \leq (3-\eta)/(1-\eta) \tag{41}$$

where η is the spatial accuracy control parameter. If $\eta = -1$ the solution is second-order accurate in space and if $\eta = \frac{1}{3}$ the solution is third-order accurate. In this study, the third-order scheme is used for all cases. The minmod limiter shows different characteristics according to the high-order extension parameter β. The smaller value of β preserves the monotonicity but introduces the larger numerical dissipation. Because a prior one-dimensional shock-tube study showed stable shock-capturing characteristic with $\beta = 1.25$ in Mach number range 4–5, this value is used as a standard value for the present study.

General Aspects of a Baseline Method

To find accurate and efficient numerical methods for the analysis of unsteady shock-induced combustion, some comparative numerical experiments are performed as follows. As a first step, simulations of experimental results were conducted to validate the performance of the baseline method. A constant time step is used equivalent to a CFL number of three for incoming flow, and four subiterations are performed. The computational domain is composed of a grid system with 200 grid points along the projectile surface and 300 grid points normal to the surface. The inflow boundary is set some distance in front of the oscillating bow shock. In addition to the simulation of experimental cases, numerical experiments were performed for one of the cases using the first- and second-order time-accurate schemes with a different number of subiterations to find the optimum value. Use of an approximate Jacobian splitting method is also examined to understand the adaptability of this scheme to unsteady problems.

Simulation of Experimental Results

For the purpose of validating the developed computational fluid dynamics code, Lehr's experiments of periodically oscillating shock-induced combustion[3] were numerically simulated. A stoichiometric hydrogen–air mixture was used in the experiment at 320 mmHg and 403 m/s of sonic velocity. This sonic velocity corresponds to the temperature of 293 K. The diameter of the hemispherical projectile used in the experiment is 15 mm. The considered cases are oscillating results at Mach numbers 4.18, 4.48, and 4.79. Experimentally observed oscillation frequencies are 148, 425, and 712 kHz, respectively. Figure 2 is the experimental shadowgraph for the cases of Mach number 4.18 and 4.79.

For the efficiency of computation, 2000 steps of time integration were performed initially by a first-order scheme without subiteration. After 1000 steps of integration, the oscillation begins to appear and goes to a regular cycle. The final solution after the 2000 steps of integration are used as an initial condition of the second-order integration. This first-order solution is also used as an initial condition for most of the numerical experiments performed in the present study.

The final solution of the second-order integration is obtained after 1000 more steps with four subiterations. The error norm of a subiteration was less than 1% of the initial error after the subiterations in every time step. Figures 3–5 show the local Mach number distribution of the flowfield and the temporal variation of density along the stagnation streamline for three Mach numbers. The Mach number distribution is selected for plotting because it shows most of the important flow characteristics of shock-induced combustion very clearly.

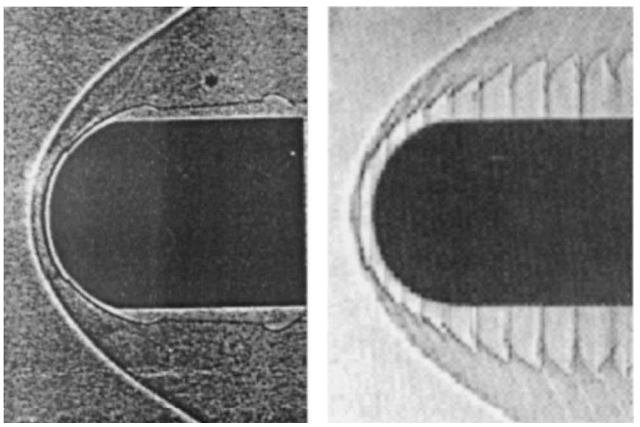

Fig. 2 Experimental shadowgraph of periodically oscillating shock-induced combustion at Mach numbers 4.18 and 4.79 (Ref. 3).

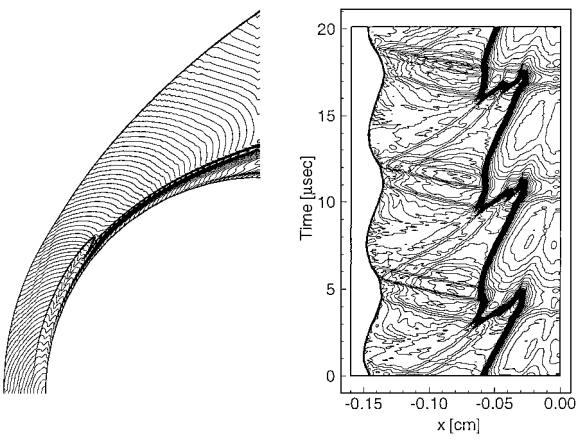

Fig. 3 Local Mach number distribution and the temporal variation of density along stagnation line for the case of $M = 4.18$.

Table 2 Comparison of the oscillation frequency of unstable shock-induced combustion

Frequency, kHz	M = 4.08	M = 4.48	M = 4.79
Experiment	148	425	712
Present result	155	426	707
Yungster and Radhakrishnan[8]	163	431	701
Matsuo and Fujiwara[5]	160	——	725
Wilson and Sussman[7]	——	——	530
Hosangadi et al.[18]	——	——	450

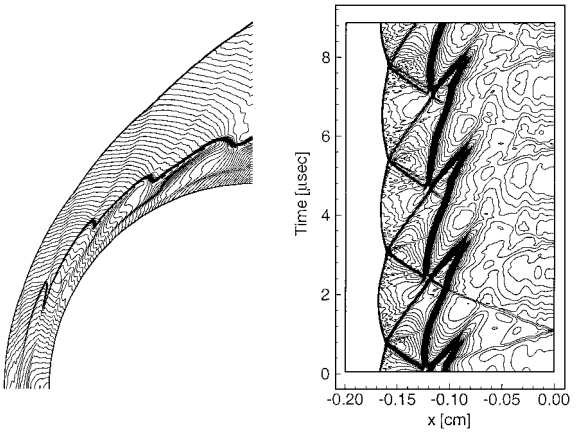

Fig. 4 Local Mach number distribution and the temporal variation of density along stagnation line for the case of M = 4.48.

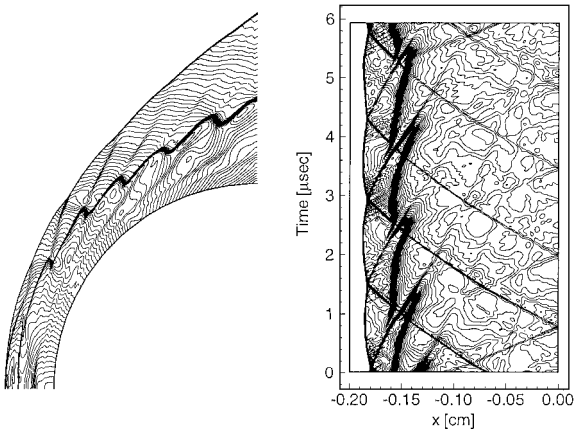

Fig. 5 Local Mach number distribution and the temporal variation of density along stagnation line for the case of M = 4.79.

The plots of Mach number distribution agree well with the experimental results, and the density history shows all of the details of the instability mechanism. The instability mechanism will not be discussed anymore because it is beyond the scope of this paper and has been discussed in previous papers.[5–7] The frequency of oscillation is obtained from these results and compared in Table 2 with experimental and numerical values obtained by previous researchers. The results of the present simulation show satisfactory agreement with experimental results even though they do not exactly agree. The chemistry mechanism used in this study is same as the one used by Yungster and Radhakrishnan[8] and Matsuo and Fujiwara,[5] and the different choice of chemistry mechanism has been known to be responsible for frequency disagreement in the results presented by Wilson and Sussman[7] and Hosangadi et al.[18] The accuracy of the chemistry mechanism will not be discussed anymore because it seems to be satisfactory, judging by the simulation of experimental results. Anyway, the baseline method could be considered to have reliable solution accuracy according to the aforementioned comparisons of the results.

On the basis of the reliability of the baseline method, the effect of different choices of numerical approaches will be discussed in the following sections. The case of Mach number 4.48 will be used as a reference case because it shows the flowfield most clearly among the three cases and also shows a sufficient number of wiggles in the reaction front and a sufficiently long induction distance between the bow shock and the reaction front, which it can be resolved with the present grid system.

Order of Integration and Number of Subiterations

The effect of the order of temporal integration and the convergence of subiteration were examined for the case of Mach number 4.48. A first-order time-accurate solution and second-order-accurate solutions with 0, 2, 4, and 10 subiterations were obtained using the same initial conditions for comparison. The initial condition is the same as the one discussed in the preceding section. All other computational conditions are fixed to that of the baseline method.

Figure 6 is the local Mach number distribution and temporal variation of density along the stagnation streamline obtained by the first-order-accurate time-integration method. The Mach number distribution shows relatively smooth variation in comparison with the second-order time-accurate solution in Fig. 4. This smoothness smears the sharpness of the waves, and some contact surfaces between the normal shock and the reaction front are not discernible in the supersonic flow region, which can be identified in second-order solution in Fig. 4. Such a trend of numerical smearing also appears in the density variation. The first-order solution seems to smear some waves but shows a very periodic oscillation, whereas the second-order solution shows sharp but numerically oscillating behavior in the postshock region.

In Fig. 7, the first-order solution shows a smooth variation of the pressure at the stagnation point whereas the second-order solution shows some overlaid high-frequency peaks on the main pressure oscillation. However, the period of oscillation seems to be unchanged in all cases with the change of the temporal accuracy of integration, except in the case of a second-order solution with zero subiterations.

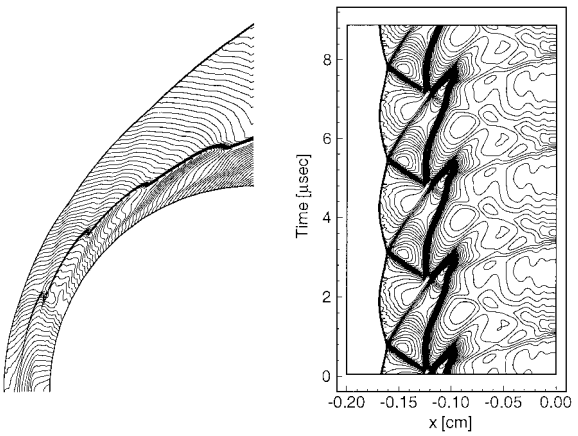

Fig. 6 Local Mach number distribution and the temporal variation of density along stagnation line for the case of M = 4.48 with first-order time integration.

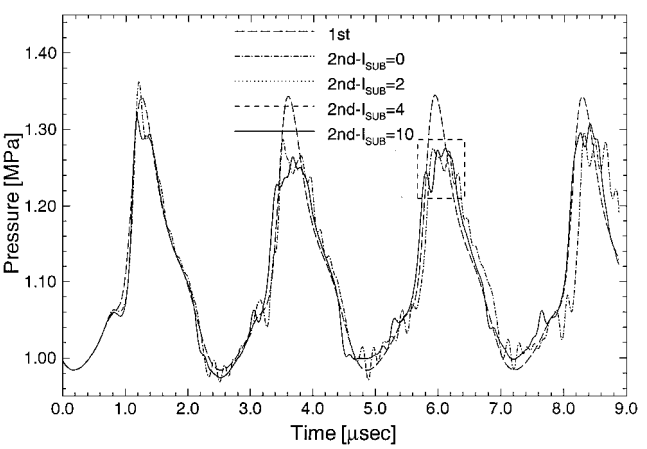

Fig. 7 Temporal variations of pressure at stagnation point by different orders of time integration and numbers of subiteration.

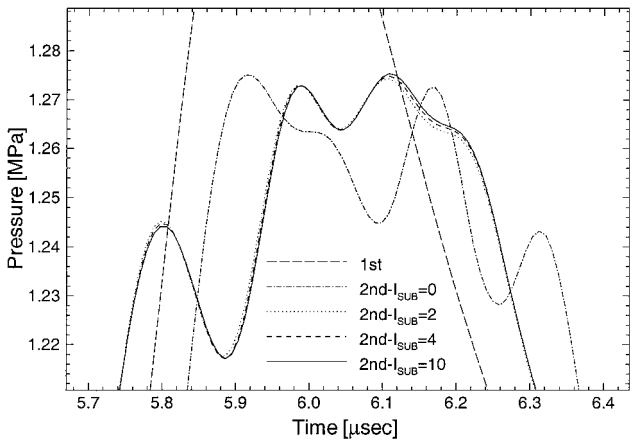

Fig. 8 Temporal variations of pressure at stagnation point by different orders of time integration and numbers of subiteration; magnified plot of dotted box in Fig. 7.

In cases when subiterations are performed, the solutions show convergence as the number of subiterations is increased, although the solution is nearly unchanged after two subiterations. This trend is shown in Fig. 8, the magnified plot of the dotted box in Fig. 7. After two subiterations, the subiteration error norm was less than 1% of the initial variation for all of the time integration steps. As a reference, the error norms were less than 1% and 0.01% for 4 subiterations and 10 subiterations. Thus, two subiterations, or the convergence criterion of 1%, is considered sufficient in this case because the computational time increases nearly proportionally to the number of subiterations.

Flux Jacobian Splitting Methods

Instead of the Steger–Warming flux Jacobian splitting method, an approximate flux Jacobian splitting could be a simple and efficient way to carry out matrix inversion of LU-factored implicit formulations.[12] This is especially true for a steady-state problem because the latter requires just one $N \times N$ matrix inversion in a lower sweep and a scalar diagonal inversion in an upper sweep, whereas the use of an exactly split Jacobian matrix requires two $(N+3) \times (N+3)$ matrix inversions in lower and upper sweeps. By the latter method, the split Jacobian matrix in Eqs. (23) and (24) is defined as

$$\boldsymbol{A}^{\pm} = \tfrac{1}{2}[\boldsymbol{A} \pm \sigma(\lambda)]$$

$$\sigma(\lambda) = \kappa\left(|U| + a\sqrt{\xi_x^2 + \xi_y^2}\right), \qquad \kappa \geq 1 \tag{42}$$

The difference of split Jacobian matrices is just a scalar value, and matrix inversion can be done much more efficiently, even though this procedure could present some difficulties in unsteady problems due to the approximation. Moreover, the upper part of the matrix inversion becomes a scalar inversion by including the chemical source Jacobian matrix $\mathbf{Z}$ only in lower part of Eq. (23), and the lower could be carried out by $N \times N$ matrix inversion by partitioning the matrix. The matrix and vector product in Eq. (24) can be also evaluated by the following simplified formulation:

$$\boldsymbol{A}^{\pm}\Delta\boldsymbol{Q} = \frac{1}{2}\begin{bmatrix} y_1 A + B\Delta q_1 \\ \vdots \\ y_N A + B\Delta q_N \\ uA + B\Delta q_{N1} + \xi_x C \\ vA + B\Delta q_{N2} + \xi_y C \\ HA + B\Delta q_{N3} + UC \end{bmatrix}$$

$$A = \xi_x \delta q_{N1} + \xi_y \delta q_{N2} - U\sum_{k=1}^{N}\Delta q_k, \qquad B = U \pm \sigma(\lambda)$$

$$C = \sum_{k=1}^{N} p_{\rho k}\Delta q_k - p_e(u\delta q_{N1} + v\delta q_{N2} - \delta q_{N3}) \tag{43}$$

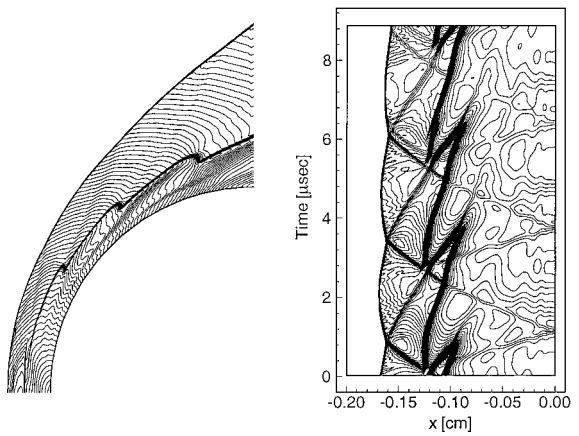

Fig. 9 Local Mach number distribution and temporal variation of density along stagnation line for the case of $M = 4.48$, with approximate Jacobian matrix splitting method and first-order time integration.

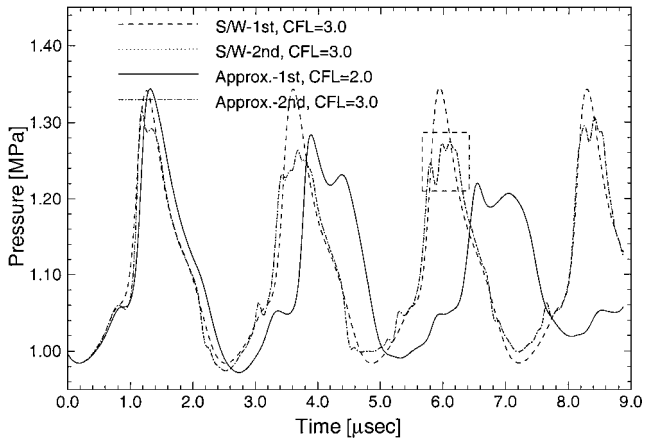

Fig. 10 Temporal variations of pressure at stagnation point by different flux Jacobian splitting methods and orders of time integration.

Because this kind of simplified formula takes only 10% of the computational time of the matrix evaluation and matrix vector product, this formula saves up to 50% of total computing time in the best case of a nonreacting flow calculation that is used as an initial condition for the unsteady simulation.

The result with the approximate Jacobian and first-order time integration is plotted in Fig. 9. In this case, the time step equivalent to a CFL number of two is used because the CFL number of three shows an instability problem. With the exception of the time step, all of the computational conditions are fixed to that of the baseline method. The Mach number distribution shows a similar diffusive manner as that in Fig. 6. Worse yet is that the periodicity begins to break in density variation. A temporally lagged solution is shown at the final distribution of the Mach number, that is, the wiggles of the combustion front are located at different positions then those shown in Figs. 4 or 6. This trend can be also found in Fig. 10, which shows the pressure variation at the stagnation point.

However, the solution is improved by using second-order time integration with four subiterations. A time step equivalent to a CFL number of three was available in this case, and the solution shows nearly the same quality as that obtained using the Steger–Warming flux Jacobian splitting method, as shown in Fig. 11. Thus, it is understood from this result that the approximation of the left-hand-side matrix would not be a significant matter if sufficient convergence could be attained. However, it is hard to say that approximate splitting is more efficient than the exact splitting method because two subiterations seem to be sufficient in the case of the Steger–Warming Jacobian splitting method. The time needed for the case of the Steger–Warming Jacobian with two subiterations is 34.24 s/iteration, and the time needed for the case of the approximate Jacobian with four subiterations is 34.90 s/iteration on a DEC

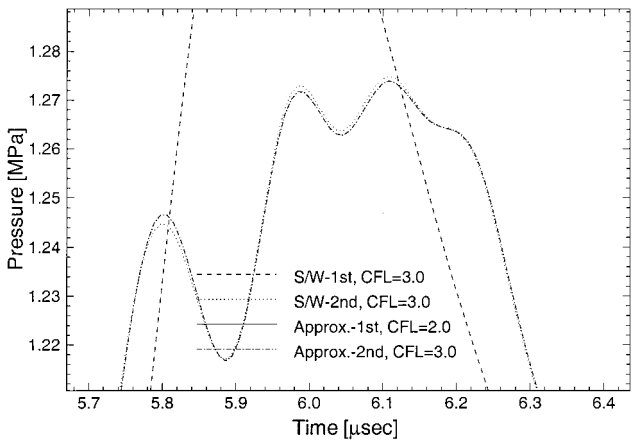

Fig. 11 Temporal variations of pressure at stagnation point by different flux Jacobian splitting methods and orders of time integration; magnified plot of dotted box in Fig. 10.

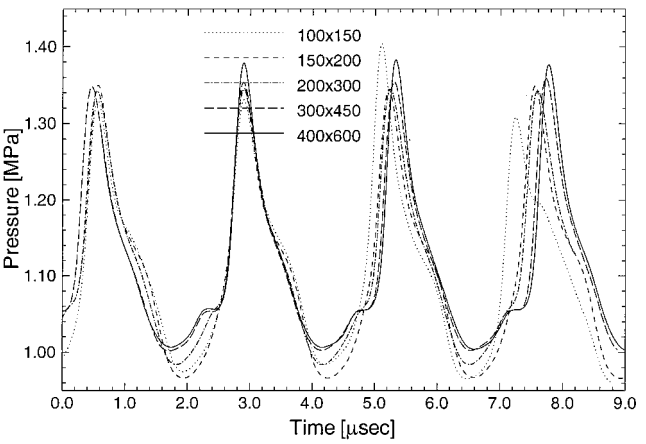

Fig. 12 Comparison of temporal variations of pressure at stagnation point for different grid systems; reference time is translated to match the time of second pressure peaks.

personal workstation. The computer is composed of a 500-MHz Alpha 21164 microprocessor with 1 MB of L2 cache and 128 MB of main memory.

Grid Refinement Study

A grid refinement study was carried out for five grid systems as an extension of the considerations on spatial discretization. The computations were performed by the first-order time integration with the same time step size used in the baseline method. All other conditions were fixed at those of the baseline method as well. The resulting pressure history is plotted in Fig. 12 for comparison. Because it is not possible to use the same initial conditions for different grid systems, the pressure curves are translated to match the time of the second pressure peaks.

The periodicity of the solution is reasonably captured in all grid systems. The frequency of oscillation is smallest for the 400×600 grid, and other results show the trend of convergence to the results of the 400×600 grid system. The deviation of the oscillation frequency is within 2% error. This trend says that the coarse grid resolution may result in a high oscillation frequency, which may be considered to be in connection with artificial damping studied in the limiter function section in part 2 of this paper,[19] in which the steepest method (having smallest numerical damping) shows the smallest frequency. Even though the result of the 100×150 grid system shows a reasonable solution in Fig. 12, the 150×200 grid system is the smallest grid system that is adequate for capturing the oscillatory behavior of shock-induced combustion, as shown in

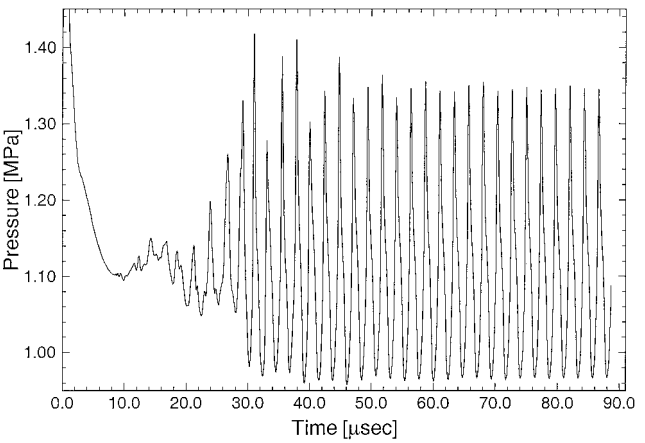

Fig. 13 Temporal variations of pressure at stagnation point by using a 150×200 grid system.

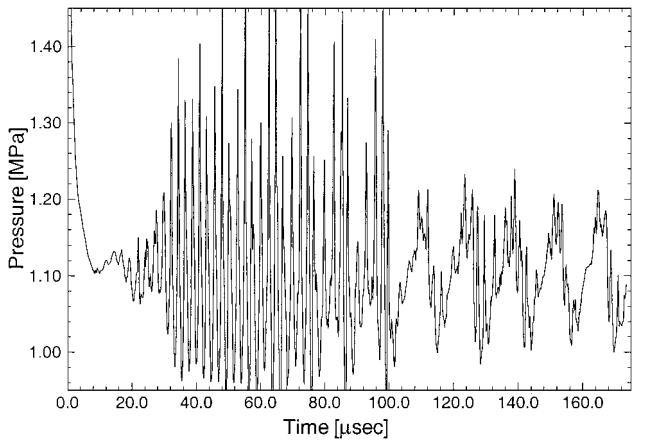

Fig. 14 Temporal variations of pressure at stagnation point by using a 100×150 grid system.

Fig. 13. The periodicity of solution breaks down in the 100×150 grid system, as plotted in Fig. 14, if more time passes.

Conclusions

A fully implicit and time-accurate computational fluid dynamic code is developed for the analysis of unsteady reactive flow systems. As a baseline method, an iterative fully implicit algorithm is used for time integration, and a third-order-accurate upwind scheme is used for spatial discretization. Periodically oscillating shock-induced combustion phenomena were considered as validation problems, and comparison with experimental results shows the validity of the baseline method.

A comparative study of numerical methods is made as a developing process of an efficient computational fluid dynamics code. The first-order-accurate time-integration method results in a spatially diffusive solution, and the periodicity of the solution is preserved well. For the iterative solution of second-order accuracy, two subiterations seem to be sufficient with the Steger–Warming formulation of the flux Jacobian matrix. The approximate splitting of the flux Jacobian matrix results in a nearly same solution as that of the baseline method, although the approximate splitting shows a diffusive and time-lagging solution without or with a small number of subiterations. Thus, the approximation of the implicit part would not be a matter of importance if a sufficient number of subiterations were carried out for convergence.

From the grid refinement study, the 100×150 grid system seems to be insufficient for the reproduction of the periodic solution. A 150×200 grid system solution would be the smallest for the stable periodic solution, although the use of a finer grid exhibits a converging trend to a smaller frequency solution.

Acknowledgments

This research is supported by the Turbo and Power Machinery Research Center and the Korea Science and Engineering Foundation under Grant 971-1005-031-2.

References

[1]Shepherd, J. E., "Detonation Waves and Propulsion," *Combustion in High-Speed Flows*, edited by J. Buckmaster, T. L. Jackson, and A. Kumar, Kluwer, Dordrecht, The Netherlands, 1994, pp. 373–420.

[2]Hertzberg, A., Bruckner, A. P., and Bogdanoff, D. W., "Ram Accelerator: A New Chemical Method for Accelerating Projectiles to Ultrahigh Velocities," *AIAA Journal*, Vol. 26, No. 2, 1988, pp. 195–203.

[3]Lehr, H. F., "Experiment on Shock-Induced Combustion," *Astronautica Acta*, Vol. 17, Nos. 4 and 5, 1972, pp. 589–597.

[4]Toong, T. Y., "Chapter 10. Mechanisms of Combustion Instability," *Combustion Dynamics: The Dynamic of Chemically Reacting Fluids*, McGraw–Hill, New York, 1983, pp. 221–277.

[5]Matsuo, A., and Fujiwara, T., "Numerical Simulation of Shock-Induced Combustion Around an Axisymmetric Blunt Body," AIAA Paper 91-1414, June 1991.

[6]Matsuo, A., Fujii, K., and Fujiwara, T., "Flow Features of Shock-Induced Combustion Around Projectile Traveling at Hypervelocities," *AIAA Journal*, Vol. 33, No. 6, 1995, pp. 1056–1063.

[7]Wilson, G. J., and Sussman, M. A., "Computation of Unsteady Shock-Induced Combustion Using Logarithmic Species Conservation Equations," *AIAA Journal*, Vol. 31, No. 2, 1993, pp. 294–301.

[8]Yungster, S., and Radhakrishnan, K., "Fully Implicit Time-Accurate Method for Hypersonic Combustion: Application to Shock-Induced Combustion Instability," AIAA Paper 94-2965, June 1994.

[9]Ahuja, J. K., Kumar, A., Singh, D. J., and Tiwari, S. N., "Simulation of Shock-Induced Combustion Past Blunt Projectiles Using Shock-Fitting Technique," *Journal of Propulsion and Power*, Vol. 12, No. 3, 1996, pp. 518–526.

[10]Gardiner, W. C., Jr., *Combustion Chemistry*, Springer–Verlag, New York, 1984.

[11]Jachimowski, C. J., "An Analytical Study of the Hydrogen–Air Reaction Mechanism with Application to Scramjet Combustion," NASA TP-2791, Feb. 1988.

[12]Shuen, S., and Yoon, S., "Numerical Study of Chemically Reacting Flows Using a Lower–Upper Symmetric Successive Overrelaxation Scheme," *AIAA Journal*, Vol. 27, No. 12, 1989, pp. 1752–1760.

[13]Roe, P. L., "Approximate Riemann Solvers, Parameter Vectors, and Difference Schemes," *Journal of Computational Physics*, Vol. 43, 1981, pp. 357–372.

[14]Yee, H. C., and Shinn, J. L., "Semi-Implicit and Fully Implicit Shock-Capturing Methods for Nonequilibrium Flows," *AIAA Journal*, Vol. 27, No. 3, 1989, pp. 299–307.

[15]Grossman, B., and Cinnella, P., "Flux Split Algorithms for Flows with Non-Equilibrium Chemistry and Vibrational Relaxation," *Journal of Computational Physics*, Vol. 88, 1990, pp. 131–168.

[16]Montagne, J. L., Yee, H. C., Klopfer, G. H., and Vinokur, M., "Hypersonic Blunt Body Computation Including Real Gas Effects," NASA TM 10074, March 1988.

[17]Hirsch, C., *Numerical Computation of Internal and External Flows*, Wiley, New York, 1990.

[18]Hosangadi, A., York, B. J., Sinha, N., and Dash, S. M., "Progress in Transient Interia Ballistic Flowfield Simulation Using Multidimensional Upwind/Implicit Numerics," AIAA Paper 93-1915, June 1993.

[19]Choi, J. Y., Jeung, I.-S., and Yoon, Y., "Computational Fluid Dynamics Algorithms for Unsteady Shock-Induced Combustion, Part 2: Comparison," *AIAA Journal*, Vol. 38, No. 7, 2000, pp. 1188–1195.

K. Kailasanath
Associate Editor